

Effects of Ohmic and ambipolar diffusion on formation and evolution of first cores, protostars and circumstellar discs

Y. Tsukamoto^{1,2}, K. Iwasaki^{2,3}, S. Okuzumi⁴, M. N. Machida⁴, and S. Inutsuka²

¹Laboratory of Computational Astrophysics, RIKEN, Saitama, Japan

²Department of Physics, Nagoya University, Aichi, Japan

³Department of Environmental Systems Science, Faculty of Science and Engineering, Doshisha University, Kyoto, Japan

⁴Department of Earth and Planetary Sciences, Tokyo Institute of Technology, Tokyo, Japan

⁵Department of Earth and Planetary Sciences, Kyushu University, Fukuoka, Japan

10 June 2015

ABSTRACT

We investigate the formation and evolution of a first core, protostar, and circumstellar disc with a three-dimensional non-ideal (including both Ohmic and ambipolar diffusion) radiation magnetohydrodynamics simulation. We found that the magnetic flux is largely removed by magnetic diffusion in the first core phase and that the plasma β of the centre of the first core becomes large, $\beta > 10^4$. Thus, proper treatment of first core phase is crucial in investigating the formation of protostar and disc. On the other hand, in an ideal simulation, $\beta \sim 10$ at the centre of the first core. The simulations with magnetic diffusion show that the circumstellar disc forms at almost the same time of protostar formation even with a relatively strong initial magnetic field (the value for the initial mass-to-flux ratio of the cloud core relative to the critical value is $\mu = 4$). The disc has a radius of $r \sim 1$ AU at the protostar formation epoch. We confirm that the disc is rotationally supported. We also show that the disc is massive ($Q \sim 1$) and that gravitational instability may play an important role in the subsequent disc evolution.

Key words: star formation – circumstellar disc – methods: hydrodynamics – smoothed particle hydrodynamics – protoplanetary disc – planet formation

1 INTRODUCTION

The molecular cloud core is the formation site of the star. Already almost half-a-century ago, Larson (1969) investigated the formation process of the protostar with one-dimensional radiation hydrodynamics simulation starting from a gravitationally unstable cloud core. An overview of the evolution obtained from that simulation is as follows: While the dust thermal emission effectively removes the thermal energy generated by the compressional heating caused by the gravitational collapse, the gas evolves almost isothermally. At $\rho \sim 10^{-13} \text{ g cm}^{-3}$, the compressional heating overtakes the radiative cooling and the gas begins to evolve adiabatically. In this adiabatic evolution phase, the temperature evolves as $T \propto \rho^{\gamma-1}$, where γ is the adiabatic index ($\gamma = 5/3$ for $T \lesssim 100$ K and $\gamma = 7/5$ for $100 \lesssim T \lesssim 2000$ K). Because this index is larger than the critical adiabatic index for spherical gravitational collapse, $\gamma_{\text{crit}} = 4/3$, the gravitational collapse temporarily halts and a quasi-hydrostatic core forms, commonly known as the *first core*. When the central temperature of the first core reaches ~ 2000 K, the hydrogen molecules begin to dissociate. This endothermic

reaction changes the effective adiabatic index to $\gamma_{\text{eff}} = 1.1$. Because this is smaller than γ_{crit} , the gravitational collapse resumes, which is known as the *second collapse*. Finally, when the molecular hydrogen is completely dissociated, the gas evolves adiabatically again and the gravitational collapse finishes. The adiabatic core formed at the centre is the protostar (or the second core). This evolution process was later confirmed, more sophisticated one-dimensional simulations (Masunaga & Inutsuka 2000; Vaytet et al. 2012, 2013).

Although, the general picture of the formation process of the protostar was established by Larson (1969) with one-dimensional simulations, multidimensional simulations are necessary to investigate important phenomena such as the formation and evolution of the circumstellar disc. After the radiation hydrodynamics simulations done by Larson (1969), it took several decades to develop and perform three-dimensional radiation hydrodynamics simulations of gravitational collapse (Whitehouse & Bate 2006; Bate 2010, 2011; Tomida et al. 2013; Tsukamoto, Machida & Inutsuka 2013; Tsukamoto et al. 2015). These studies revealed that the multi-dimensionality causes new and interesting phenomena. For example, Bate (2010) found that the bipolar

outflow from the first core can be driven by radiative feedback from the protostar. Tsukamoto et al. (2015) investigated the evolution of the circumstellar discs in the unmagnetized cloud core and found that the temperature structure of the disc is determined by diffusive radiative transfer in the radial direction in its early evolution phase.

The magnetic field is another important ingredient in the star formation process. Observations suggest that the molecular cloud cores are magnetized (e.g. Heiles & Troland 2005; Troland & Crutcher 2008). Troland & Crutcher (2008) showed that the mean value of the mass-to-flux ratio relative to the critical value, μ , of the nearby dark cloud cores is $\mu \sim 2 - 3$ and suggested that the magnetic field of the typical cloud core is relatively strong. The magnetic field drives the outflow from both the first core and the protostar. The typical velocity of the outflow is determined by the rotational velocity at the launching point ($v \sim 2$ km/s from the first core and $v \sim 20$ km/s from the protostar) (Tomisaka 2002; Machida, Inutsuka & Matsumoto 2008; Hennebelle & Fromang 2008; Price, Tricco & Bate 2012). Another important effect caused by the magnetic field is the removal of the gas angular momentum. This effect is known as *magnetic braking* (Mouschovias & Paleologou 1979). Until recently, it was believed that the disc formation is a natural consequence of the gravitational collapse of a rotating molecular cloud core. Actually, three-dimensional simulations, with a weak magnetic field or without it, show that a relatively large circumstellar disc (with a radius of several tens of AU) develops in the early phase of protostar formation (Bate 1998, 2011; Tsukamoto & Machida 2011, 2013; Tsukamoto, Machida & Inutsuka 2013) However, previous works with ideal magnetohydrodynamics (MHD) simulations have shown that the relatively strong magnetic field ($\mu \sim 1$) completely suppresses the formation of a rotationally supported disc around the protostar at its formation epoch (Mellon & Li 2008; Hennebelle & Fromang 2008).

Ideal MHD is, however, not a good approximation for the simulations of the magnetized molecular cloud core. Because the ionization degree of the cloud core is quite low, it is expected that non-ideal magnetic effects such as Ohmic diffusion, Hall effect, and ambipolar diffusion play important roles during the formation and evolution of the circumstellar disc.

The influence of non-ideal magnetic effects on the disc formation is still controversial. Li, Krasnopolsky & Shang (2011) investigated the influences of the non-ideal magnetic effects. They pointed out that ambipolar diffusion is the dominant diffusion process of the magnetic field and concluded that neither Ohmic nor ambipolar diffusion weakens the magnetic braking and that the disc formation is still strongly suppressed even with the magnetic diffusion. On the other hand, Machida, Inutsuka & Matsumoto (2011) showed that a relatively large disc of about a few tens of AU in size forms in the early phase of the protostar formation although they considered only Ohmic diffusion.

The discrepancy could come from the difference in the initial conditions and the treatment of the inner boundary (or a sink at the centre) of the simulations. In the simulations of Mellon & Li (2008) and Li, Krasnopolsky & Shang (2011), the inner boundary or sink is set from the beginning of the simulations. In such a set-up, the simu-

lations cannot follow the evolution of a first core which is mainly supported by gas pressure and not necessarily by rotation. Although the first core is a transient object, its density is high enough that the magnetic flux is efficiently removed from the first core during its evolution (Dapp, Basu & Kunz 2012). Furthermore, it is suggested that the greater part of the first core directly becomes the circumstellar disc (Machida & Matsumoto 2011) just after the protostar formation. Therefore, calculating the first-core phase correctly in the simulations is crucial to investigate the very early phase of disc evolution. On the other hand, Machida, Inutsuka & Matsumoto (2011) used sink cells with “threshold density”. In their simulations, the sink cell takes in the gas when its density becomes larger than the threshold density. In this case, the gas whose density is smaller than the threshold density can reside inside or around the sink cell regardless of whether the gas is rotationally supported or not. This treatment may also affect the disc evolution process. Machida, Inutsuka & Matsumoto (2014) showed that the sink treatment (its radius and the threshold density) significantly affects the formation and evolution of the circumstellar disc.

To reveal the realistic formation and evolution processes of the first core, the protostar, and the circumstellar disc, appropriate treatment of the radiation transfer in the simulation is crucial, because the magnetic diffusion coefficients are functions of temperature. The previous studies with MHD simulations mentioned above do not include radiation transfer and employ a simplified equation of state (EOS) which mimics the temperature evolution of the *centre* of the cloud core. We call this the barotropic approximation. The simulations with radiation transfer, however, have shown that the temperature structures in the first core or around the protostar are strikingly different from those expected from the barotropic approximation (Whitehouse & Bate 2006; Bate 2010; Tomida et al. 2013; Tsukamoto et al. 2015).

Three-dimensional simulations which include both the magnetic field and radiation transfer have not been successful until recently. Tomida et al. (2013) was the first to succeed with such a simulation with a grid code and found that the Ohmic diffusion alters the structure around the protostar significantly. With ideal radiation magnetohydrodynamics (RMHD) simulations using the smoothed particle hydrodynamics (SPH) method, Bate, Tricco & Price (2014) also investigated the formation and evolution of the protostar, especially the long-term evolution of the bipolar jets driven around the protostar. They showed that the jets heat up the gas in the envelope after they break up the remnant of the first core. Such a radiative heating process may affect the ionization degree of the gas and change the magnetic diffusion coefficients. However, Bate, Tricco & Price (2014) did not consider magnetic diffusion processes.

As pointed out in previous studies (Li, Krasnopolsky & Shang 2011), it is expected that ambipolar diffusion will play a role during the formation process of the protostar and the disc around it. Very recently, Tomida, Okuzumi & Machida (2015) conducted a simulation with both Ohmic and ambipolar diffusion. However, they only calculated the evolution until the end of the first core phase with ambipolar diffusion and the effect of the ambipolar diffusion is still unclear.

In this paper, we investigate the formation of the first

core, protostar, and the circumstellar disc using a three-dimensional non-ideal RMHD simulation. We employ the SPH method and use it to produce the first results of the three-dimensional non-ideal RMHD simulations with SPH. Here, we focus on the effects of magnetic (Ohmic and ambipolar) diffusion, but do not include the Hall effect. To avoid the numerical artefact caused by the sink, we do not introduce it, but rather investigate the structure around the protostar to determine whether the formation of the circumstellar disc is possible at the very early phase of protostar formation. This paper is organized as follows: In §2, we briefly describe the non-ideal magnetohydrodynamic effects. In §3, we describe the numerical method and initial conditions for the simulations, the results of which are given in §4, and then summarized and discussed in §5.

2 NON-IDEAL MAGNETOHYDRODYNAMIC EFFECTS

The ionization degree in the molecular cloud core is quite low and the gas can be regarded as weakly ionized plasma. In weakly ionized plasma, the microscopic collisions between neutral, positively-charged, and negatively-charged particles produce finite conductivity and non-ideal magnetohydrodynamic effects, or in short, non-ideal effects arise.

The non-ideal effects appear as the correction terms in the induction equation. They can be derived by calculating the drift velocity of the charged particles. Here, we derive the induction equation for the weakly ionized plasma according to Wardle & Ng (1999) and Wardle (2007).

We start with

$$\frac{\partial \mathbf{B}}{\partial t} = -c \nabla \times \mathbf{E}, \quad (1)$$

$$\mathbf{J} = \frac{c}{4\pi} \nabla \times \mathbf{B}. \quad (2)$$

where \mathbf{B} is the magnetic field, \mathbf{J} is the current density, \mathbf{E} is the electric field, and c is the speed of light. By the Lorentz transformation to the rest frame of the fluid (that is essentially the rest frame of bulk of neutral particles), the electric field becomes

$$\mathbf{E}' = \mathbf{E} + \frac{\mathbf{v} \times \mathbf{B}}{c}. \quad (3)$$

Here, \mathbf{v} and \mathbf{E}' are the fluid velocity and the electric field in the rest frame of the fluid, respectively. The conductivity in the weakly ionized plasma can be calculated using the balance of the force that acts on the charged particles,

$$Z_j e (\mathbf{E}' + \frac{\mathbf{v}_j \times \mathbf{B}}{c}) - \gamma_j \rho m_j \mathbf{v}_j = 0. \quad (4)$$

Here, subscript j denotes the species of charged particles, $Z_j e$ is the charge, \mathbf{v}_j is the relative velocity of charged particles in the fluid rest frame, $\gamma_j = \langle \sigma v \rangle_j / (m_j + m)$ where $\langle \sigma v \rangle_j$ is the rate coefficient for momentum transfer, m_j is the mass of charged particles, m is the mean mass of neutral particles, and ρ is the density of neutral particles. Note that, in the weakly ionized plasma, most of the particles are neutral and the inertia of the charged particles and the collisions with other charged particles are negligible. Note also that, under the MHD approximation, the difference between the magnetic field and the current density in computation frame and those in the rest frame is negligible. We assumed

the local charge neutrality $\sum_j n_j Z_j = 0$. By inverting (4) for \mathbf{v}_j and calculating the current density, $\mathbf{J} = \sum_j n_j Z_j e \mathbf{v}_j$, we obtain

$$\mathbf{J} = \sigma_O \mathbf{E}' + \sigma_H \hat{\mathbf{B}} \times \mathbf{E}' - (\sigma_P - \sigma_O) \hat{\mathbf{B}} \times \hat{\mathbf{B}} \times \mathbf{E}', \quad (5)$$

where

$$\sigma_O = \frac{ec}{B} \sum_j n_j Z_j \beta_j, \quad (6)$$

$$\sigma_H = \frac{ec}{B} \sum_j \frac{n_j Z_j}{1 + \beta_j^2}, \quad (7)$$

$$\sigma_P = \frac{ec}{B} \sum_j \frac{n_j Z_j \beta_j}{1 + \beta_j^2}, \quad (8)$$

(9)

are the Ohmic, Hall, and Pedersen conductivities, respectively. Here, $\beta_j = Z_j e B / (m_j c \gamma_j \rho)$ is the Hall parameter which is the product of the cyclotron frequency and stopping time. Finally, by inverting equation (5) for \mathbf{E}' and using equation (1) and (3), we obtain

$$\begin{aligned} \frac{\partial \mathbf{B}}{\partial t} &= \nabla \times (\mathbf{v} \times \mathbf{B}) \\ &- \nabla \times \left\{ \eta_O (\nabla \times \mathbf{B}) + \eta_H (\nabla \times \mathbf{B}) \times \hat{\mathbf{B}} - \eta_A ((\nabla \times \mathbf{B}) \times \hat{\mathbf{B}}) \times \hat{\mathbf{B}} \right\}. \end{aligned} \quad (10)$$

This is the induction equation with non-ideal effects. The second, third, and fourth term on the right hand side of equation (10) describe the Ohmic diffusion, Hall term, and ambipolar diffusion, respectively. Here,

$$\eta_O = \frac{c^2}{4\pi \sigma_O}, \quad (11)$$

$$\eta_H = \frac{c^2 \sigma_H}{4\pi (\sigma_H^2 + \sigma_P^2)}, \quad (12)$$

$$\eta_A = \frac{c^2 \sigma_P}{4\pi (\sigma_H^2 + \sigma_P^2)} - \eta_O, \quad (13)$$

are the Ohmic, Hall, and ambipolar diffusion coefficients, respectively. In this paper, the Hall term is neglected owing to the numerical difficulty associated with it. The effect of the Hall term will be investigated in future works.

We constructed the data table of the diffusion coefficients by calculating a chemical reaction network of H_3^+ , HCO^+ , Mg^+ , He^+ , C^+ , H^+ , e^- in gas phase and the positively-charged, neutral, and negatively-charged dust grain of uniform size using the methods described in Nakano, Nishi & Umebayashi (2002) and Okuzumi (2009). We assumed that the dust to gas ratio is 10^{-2} . We also assumed that the dust grain size and density are $a = 3.5 \times 10^{-2} \mu\text{m}$ and $\rho_d = 2 \text{ g cm}^{-3}$, respectively. We considered non-thermal ionization by the cosmic rays and thermal ionization in our calculations. The cosmic-ray ionization rate was fixed to be $\xi_{\text{CR}} = 10^{-17} \text{ s}^{-1}$. When the temperature reaches $T \sim 1000 \text{ K}$, thermal ionization is the dominant source of ionization. In this paper, we consider the effect of the thermal ionization by considering the thermal ionization of potassium. The coupling between the magnetic field and the gas quickly recovers around $T \sim 1000 \text{ K}$ because the thermal ionization provides a sufficient ionization degree.

In figure 1, we show the Ohmic and ambipolar diffusion coefficients under the typical evolution of the gas. To make figure 1, we assumed that the temperature and magnetic

field change as,

$$B(\rho) = 100 \left(\frac{\rho}{10^{-15} \text{ g cm}^{-3}} \right)^{2/3} \mu\text{G},$$

$$T(\rho) = 10 \left\{ 1 + \left(\frac{\rho}{10^{-13} \text{ g cm}^{-3}} \right)^{2/5} \right\} \text{K}. \quad (14)$$

The figure shows that the diffusion coefficients suddenly drop around $\rho = 5 \times 10^{-9} \text{ g cm}^{-3}$ where the temperature is about $T = 1000 \text{ K}$ and the ionization degree quickly increases owing to the thermal ionization of potassium.

3 NUMERICAL METHOD AND INITIAL CONDITIONS

In this study, we solve the non-ideal radiation magnetohydrodynamics equations with self-gravity,

$$\frac{D\mathbf{v}}{Dt} = -\frac{1}{\rho} \left\{ \nabla \left(P + \frac{1}{2} B^2 \right) - \nabla \cdot (\mathbf{B}\mathbf{B}) \right\} - \nabla \Phi, \quad (15)$$

$$\frac{D}{Dt} \left(\frac{\mathbf{B}}{\rho} \right) = \left(\frac{\mathbf{B}}{\rho} \cdot \nabla \right) \mathbf{v} - \frac{1}{\rho} \nabla \times \left\{ \eta_O (\nabla \times \mathbf{B}) - \eta_A (\nabla \times \mathbf{B}) \times \hat{\mathbf{B}} \times \hat{\mathbf{B}} \right\}, \quad (16)$$

$$\frac{D}{Dt} \left(\frac{E_r}{\rho} \right) = -\frac{\nabla \cdot \mathbf{F}_r}{\rho} - \frac{\nabla \mathbf{v} : \mathbb{P}_r}{\rho} + \kappa_P c (a_r T_g^4 - E_r), \quad (17)$$

$$\frac{D}{Dt} \left(\frac{e}{\rho} \right) = -\frac{1}{\rho} \nabla \cdot \left\{ \left(P + \frac{1}{2} B^2 \right) \mathbf{v} - \mathbf{B} (\mathbf{B} \cdot \mathbf{v}) \right\} - \kappa_P c (a_r T_g^4 - E_r) - \mathbf{v} \cdot \nabla \Phi - \frac{1}{\rho} \nabla \cdot \left[\left\{ \eta_O (\nabla \times \mathbf{B}) - \eta_A (\nabla \times \mathbf{B}) \times \hat{\mathbf{B}} \times \hat{\mathbf{B}} \right\} \times \mathbf{B} \right], \quad (18)$$

$$\nabla^2 \Phi = 4\pi G \rho. \quad (19)$$

Here, ρ is the gas density, \mathbf{v} is the velocity, \mathbf{B} is the magnetic field, $\hat{\mathbf{B}}$ is the unit directional vector of the magnetic field, P is the gas pressure, E_r is the radiation energy, \mathbf{F}_r is the radiation flux, \mathbb{P}_r is the radiation pressure, T_g is the gas temperature, κ_P is the Plank mean opacity, $e = \rho u + \frac{1}{2} (\rho \mathbf{v}^2 + \mathbf{B}^2)$ is the total energy with u specific internal energy, and Φ is the gravitational potential. Parameters, a_r and G are the radiation and gravitational constants, respectively.

We adopt the gray approximation (frequency-integrated radiation transfer) and we assume local thermodynamic equilibrium (LTE). To close the equations for radiation transfer, we employ flux-limited diffusion (FLD) approximations,

$$\mathbf{F}_r = \frac{c\lambda}{\kappa_R \rho} \nabla E_r, \quad \lambda(R) = \frac{2 + R}{6 + 2R + R^2},$$

$$R = \frac{|\nabla E_r|}{\kappa_R \rho E_r}, \quad \mathbb{P}_r = \mathbb{D} E_r,$$

$$\mathbb{D} = \frac{1 - \chi_{\parallel}}{2} + \frac{3\chi_{\perp} - 1}{2} \mathbf{n} \otimes \mathbf{n}, \quad \chi = \lambda + \lambda^2 R^2,$$

$$\mathbf{n} = \frac{\nabla E_r}{|\nabla E_r|}.$$

Here, κ_R is the Rosseland mean opacity. FLD is a diffusion scheme which is designed to maintain the causality of $|\mathbf{F}_r| < cE_r$. It is suitable for optically thick gas

owing to its diffusive nature. In this paper, we use the SPH method to investigate the formation of a protostar and disc. The SPH method can be easily implemented and is suitable for simulations which treat the large dynamic range because of its adaptive nature. The ideal MHD part was solved by adopting the Godunov smoothed particle magnetohydrodynamics (GSPMHD) method in which the Godunov method and the method of characteristics are used to calculate the interactions between the particles instead of artificial dissipation terms (Iwasaki & Inutsuka 2011). The divergence-free constraint on the magnetic field was maintained using the hyperbolic divergence cleaning method for GSPMHD (Iwasaki & Inutsuka 2013). The radiative transfer was treated by the FLD-SPH method (Whitehouse & Bate 2004; Whitehouse, Bate & Monaghan 2005). We treated Ohmic and ambipolar diffusion with the method described by Tsukamoto, Iwasaki & Inutsuka (2013) and Wurster, Price & Ayliffe (2014), respectively. Both diffusion processes were accelerated by super time stepping method (Alexiades, Amiez & Gremaud 1996). To calculate the self-gravity, we adopted the Barnes-Hut tree algorithm with opening angle of $\theta = 0.5$ (Barnes & Hut 1986). We do not use the individual time-steps and the particles are updated simultaneously.

We adopted the tabulated EOS used in Tomida et al. (2013), in which the internal degrees of freedom and chemical reactions of seven species H_2 , H , H^+ , He , He^+ , He^{++} , e^- are included. We assumed that the hydrogen and helium mass fractions were $X = 0.7$ and $Y = 0.28$, respectively. The dust opacity table was obtained from Semenov et al. (2003) and the gas opacity table was obtained from Ferguson et al. (2005). The resistive model is described in §2.

We modelled the initial cloud core using an isothermal uniform gas sphere. The initial mass and temperature of the core were fixed at $1 M_{\odot}$ and 10 K , respectively, with an initial core radius of $R \sim 3.0 \times 10^3 \text{ AU}$. The core is initially rigidly rotating with an angular velocity of $\Omega_0 = 2.2 \times 10^{-13} \text{ s}^{-1}$. The product of the angular velocity and the free-fall time is $t_{\text{ff}} \Omega_0 = 0.19$. The initial magnetic field was uniform and parallel to the rotation (z -) axis with a strength of $B_0 = 1.7 \times 10^2 \mu\text{G}$. The corresponding initial mass-to-flux ratio relative to the critical value was $\mu = (M/\Phi)/(M/\Phi)_{\text{crit}} = 4$ where $\Phi = \pi R^2 B_0$. We adopted a critical mass-to-flux ratio of $(M/\Phi)_{\text{crit}} = (0.53/3\pi)(5/G)^{1/2}$ suggested by Mouschovias & Spitzer (1976). The initial cores were modelled with about 10^7 SPH particles. The boundary conditions of radiation transfer were introduced by fixing the gas temperature to be 10 K when the gas density was less than $2.0 \times 10^{-17} \text{ g cm}^{-3}$.

We performed three simulations with and without Ohmic and ambipolar diffusion. The model names and the diffusion processes included in each model are summarized in Table 1.

4 SIMULATION RESULTS

4.1 Evolution at the centre of the cloud core

To investigate how the magnetic field evolves during the gravitational collapse, we show the evolution of the central

Table 1. The model names and the magnetic diffusion they include. “Yes” means that the corresponding magnetic diffusion is included while a “No” means that it is not.

Model	Ohmic diffusion	Ambipolar diffusion
1	No	No
2	Yes	No
3	Yes	Yes

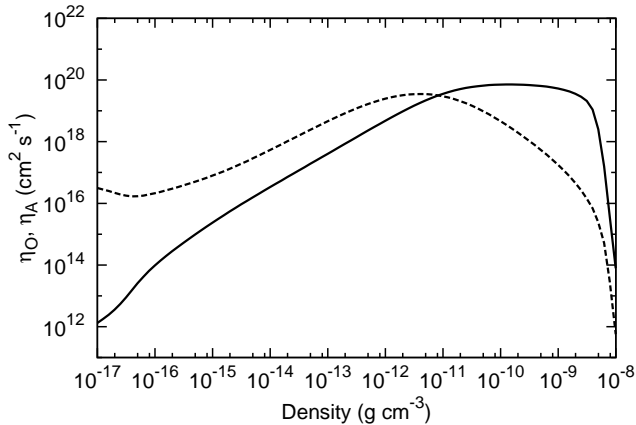


Figure 1. Diffusion coefficients, η_O (solid) and η_A (dotted) as a function of density. For this plot, we assumed that the temperature and magnetic field are functions of density (see eq. (14)).

magnetic field as a function of the central density in figure 2. At first, the magnetic field evolves as $B_c \propto \rho_c^{2/3}$. This evolution is expected from a spherically symmetric collapse during which the central magnetic field evolves as $B_c \propto R^{-2}$ due to the conservation of the magnetic flux, where R is the radius of the cloud. On the other hand, the central density evolves as $\rho_c \propto R^{-3}$ or, equivalently, $R \propto \rho_c^{-1/3}$. Thus, $B_c \propto R^{-2} \propto \rho_c^{2/3}$. The increase in the magnetic field almost stops ($B_c \propto \rho_c^0$) at $10^{-15} \lesssim \rho_c \lesssim 10^{-14} \text{ g cm}^{-3}$ because the Lorentz force becomes comparable to the gravitational force and the gas moves almost parallel to the magnetic field. The z -component of the magnetic field still dominates other components and the gas moves almost vertically. As a result, a sheet-like structure (or pseudo disc) forms. When the central density reaches $\rho_c \sim 10^{-13} \text{ g cm}^{-3}$, the central magnetic field evolves as $B_c \propto \rho_c^{1/2}$ which indicates that the collapse becomes sheet-like. In the gravitationally collapsing isothermal sheet (whose scale-height is $H = c_s^2/(G\Sigma) = c_s/\sqrt{G\rho_c}$), the central magnetic field and density evolves as $B_c \propto R^{-2}$ and $\rho_c \propto R^{-2}H^{-1} \propto R^{-4}$ and hence $B_c \propto \rho_c^{1/2}$.

Once the central density exceeds $\rho \sim 10^{-12} \text{ g cm}^{-3}$, the magnetic diffusions becomes effective and the magnetic freezing is no longer valid for resistive models. The magnetic flux is removed from the central part and the difference between the ideal model and resistive models can be seen. The central magnetic field of model 1 (the ideal model) is about sixty times larger than that of model 3 (with Ohmic and ambipolar diffusion) when the central density reaches $\rho_c \sim 10^{-9} \text{ g cm}^{-3}$. Around the $\rho_c \sim 10^{-9} \text{ g cm}^{-3}$, the magnetic diffusion becomes ineffective again owing to the ther-

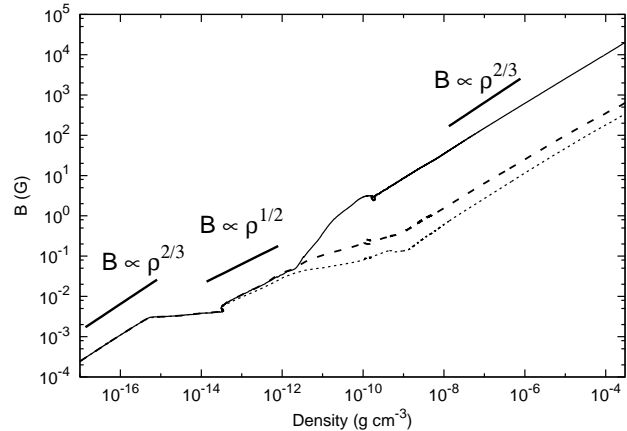


Figure 2. The evolution of the central magnetic field as a function of central density. The solid, dashed, and dotted lines show the results of model 1 (ideal), model 2 (with Ohmic diffusion), and model 3 (with Ohmic and ambipolar diffusion), respectively. Differences between the models can be seen when the central density exceeds $\rho_c > 10^{-12} \text{ g cm}^{-3}$ and magnetic diffusion becomes effective.

mal ionization and the flux freezing recovers in the resistive models. This causes $B_c \propto \rho_c^{2/3}$ again.

4.2 Structure of the first core

When the central density reaches $\rho_c \sim 10^{-13} \text{ g cm}^{-3}$, the gas becomes opaque and the compressional heating due to the gravitational contraction cannot radiate away efficiently. As a result, the gas evolves adiabatically and a pressure-supported core, the first core, forms. The first core phase lasts until the central temperature becomes $T_c \sim 2000 \text{ K}$ (or $\rho_c \sim 10^{-8} \text{ g cm}^{-3}$) at which point the dissociation of hydrogen molecules begins. The durations of the first core phase are about 620 years for model 1, 810 years for model 2, and 940 years for model 3. The first core phase is defined as the phase in which the central density is $10^{-13} \text{ g cm}^{-3} < \rho_c < 10^{-8} \text{ g cm}^{-3}$. The difference in the duration is due to the rotation of the first core.

To investigate the structure in and around the first core, we show the cross sections of the density, gas temperature, and plasma β around the first core in the $y = 0$ plane in figure 3 at the end of the first core phase ($\rho_c \sim 3 \times 10^{-9} \text{ g cm}^{-3}$). The plasma β is defined as $\beta = P_{\text{gas}}/P_{\text{mag}}$ where P_{gas} and P_{mag} are the gas pressure and magnetic pressure, respectively. Note that the box size of the density cross sections is four times that of the other cross sections to compare the outflow structures of each model.

To obtain the cross section and the profiles, the phys-

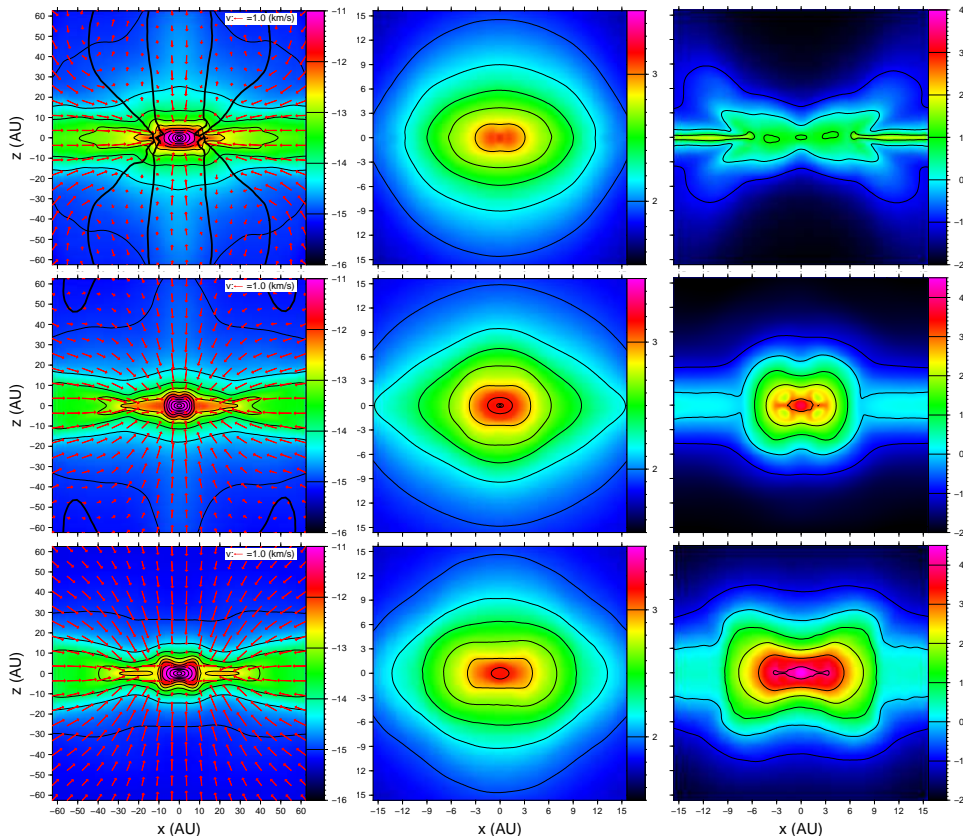


Figure 3. The cross sections of the density, gas temperature, and plasma β (from left to right) around the first core in the $y = 0$ plane. The top row corresponds to model 1, the middle row to model 2, and the bottom row to model 3. The thin black lines show the contour of each quantity, while the thick black lines in the density cross sections show the $|v_z| = 0$ contour. This traces the outflow regions. The red arrows in the density cross sections show the velocity field. The box size of the density cross sections is four times larger than the other cross sections to show the outflow structures. The color bars of the density, temperature, and plasma β show $\log(\rho [g\text{ cm}^{-3}])$, $\log(T [\text{K}])$, and $\log(\beta)$, respectively.

ical quantities are needed at grid points. In this paper, the physical quantities are calculated at grid points through,

$$f(\mathbf{x}_{\text{grid}}) = \frac{\sum_j m_j \frac{f(\mathbf{x}_j)}{\rho_j} W(\mathbf{x}_{\text{grid}} - \mathbf{x}_j, h_j)}{\sum_j m_j \frac{1}{\rho_j} W(\mathbf{x}_{\text{grid}} - \mathbf{x}_j, h_j)}. \quad (20)$$

In the left panels, we show the density cross section. The thick black solid lines show the $v_z = 0$ contour and trace the outflow structure. The outflow formed in both model 1 and 2, but did not in model 3 at the epochs. Although the outflow did not form in model 3, we confirmed that the outflow does form in a simulation with both Ohmic and ambipolar diffusion when the initial rotation of the cloud core is slightly larger than in the model 3. Therefore, we conclude that the magnetic resistivity delays the formation of the outflow rather than suppressing it. In our results, both the magneto-centrifugal force and the magnetic pressure play a role in driving the outflow.

In the middle panels, we show the temperature cross section around the first core. The high temperature ($T \sim 1000$ K) regions with radius of $r \sim 5$ AU are formed at the centre due to the radiative transfer. The high temperature region is extended compared to the case in which the barotropic EOS is adopted. Because the thermal ionization becomes effective at $T \sim 1000$ K, the coupling between the

magnetic field and the gas recovers in the relatively large part of the first core when the radiative transfer is taken into account. This recoupling causes the amplification of the magnetic field inside the first core due to the rotation.

In the right panels, we show the cross section of the plasma β . Because of the magnetic diffusion, the magnetic flux is efficiently removed from the first core in the resistive models. Thus, in the resistive models, $\beta \gtrsim 10^3$ at the centre of the first core while in the ideal model, $\beta \sim 10$. After the removal of the magnetic flux, the coupling between the gas and the magnetic field recovers at the central region of the first core owing to the thermal ionization and the magnetic field in the first core is reamplified by the rotation. As a result, the plasma β around the centre slightly decreases in the resistive models. This amplification is clearly seen in the middle right panel.

Figure 4 shows the profiles of the density, gas temperature, and plasma β at the same epoch of figure 3. In all models, the central density and the central temperature of the first core are $\rho_c \sim 3 \times 10^{-9} g\text{ cm}^{-3}$ and $T_c \sim 10^3$ K, respectively. The density and temperature profiles show that the first cores formed in each model have very similar structures. This is because the angular momenta of the first cores are not significantly different and the structural difference caused by rotation is negligible. The density on the x -axis

is larger than that on the z -axis outside of the first core because the pseudo disc has formed in the x direction. On the other hand, the temperature profiles along the x and z -axis do not differ significantly and the temperature structure is hence almost spherically symmetric.

Due to the magnetic diffusions, the plasma β in the central region of the first core differs significantly between the ideal model and the resistive models. In model 1, the plasma β inside the first core is $\beta \sim 10$ and almost constant in the x direction. In the model 2, the plasma β at the centre of the first core becomes $\beta \sim 6 \times 10^3$. This is hence about three orders magnitude greater than for the ideal model. The magnetic flux removed from the first core piles up around it and the plasma β on the x -axis becomes smaller than the ideal model at the perimeter of the first core ($x \sim 10$ AU). In model 3, the plasma β at the centre of the first core becomes $\beta \sim 6 \times 10^4$, which is much higher than for the model 2. In the z direction, the plasma β quickly decreases in all models because of the large density gradient in this direction and the magnetic field amplification by the first core rotation. Because the plasma β is larger than 10 inside the first core, the magnetic pressure does not affect the pressure support in the first core.

A notable difference between models 2 and 3 is the plasma β in the x direction *at the perimeter* of the first core. In the model 2, only Ohmic diffusion is considered. The Ohmic diffusion coefficient is an increasing function of density and does not depend on the magnetic field. Roughly speaking, the Ohmic diffusion does not play a role when $\rho \lesssim 10^{-13}$ g cm $^{-3}$ (Machida, Inutsuka & Matsumoto 2007). Because the density of the first core is $\rho \gtrsim 10^{-13}$ g cm $^{-3}$, the magnetic flux piles up outside the first core. By this pile-up, the plasma β beyond the first core in model 2 is $\beta \sim 1$ around $x = 10$ AU and becomes much smaller than for model 1 at larger x . In model 3, the ambipolar diffusion is included as well. The diffusion coefficient of the ambipolar diffusion is a function of the magnetic field and does not depend strongly on the density. Therefore, it is expected that the pile-up of the magnetic flux is smoothed by the ambipolar diffusion. Actually, the region of small plasma β ($\beta \sim 1$) in the x direction broadens in the right panel. This difference can also be seen in the right panels of figure 4.

In figure 5, we show the infall and rotation velocities along the x -axis and the infall velocity along the z -axis. The infall velocity along the x -axis is larger than that along the z -axis and the density on the x -axis is also much higher than on the z -axis at the surface of the first core ($x, z \sim 10$ AU). Therefore, the mass accretion onto the first core is asymmetric and is maximal in the horizontal direction.

The rotation velocity v_ϕ reaches its maximum value at $x \sim 2$ AU in models 2 and 3. Inside this radius, the velocity profile obeys the rigid rotation relation, $v_\phi \propto x$. Note that a rigid rotation is expected when the density is constant because $v_\phi \propto \sqrt{M_r/r} \propto \sqrt{\rho_0 r^3/r} \propto r$, where M_r and ρ_0 are the mass inside r and the density, respectively. In model 2, v_ϕ sharply decreases at the $r \sim 4$ AU. This is caused by the strong magnetic braking by the piled-up magnetic field. As mentioned above, the magnetic flux piles up around the first core. Hence, the magnetic braking is locally enhanced at $r \sim 4$ AU and the rotation velocity is decreases. The profile of the model 1 also obeys the relation of $v_\phi \propto x$ for $x \lesssim 1$ AU. On the other hand, for $3 \text{ AU} \lesssim x \lesssim 10 \text{ AU}$, the

profile has a complex structure. This structure is also caused by the magnetic braking. Note that the plasma β inside the first core is still small in model 1.

In figure 6, we show the evolution of the angular momentum of the first core in relation to the central density. We define the first core as the region where $\rho > 10^{-13}$ g cm $^{-3}$. As we have seen above, the magnetic field in the first core becomes weak due to the magnetic diffusion which causes an inefficient angular momentum transfer by the magnetic braking. Thus, it is expected that the angular momentum of the first core becomes large in resistive models and it indeed becomes large when the magnetic diffusion is included. The difference in the angular momentum between model 1 and model 3 is a factor of 6 and hence, insignificant. Most of the initial angular momentum of the fluid element has already been removed during the isothermal collapse phase. With the parameters adopted in our simulations, a disc of $r \sim 100$ AU forms when the magnetic field is neglected (see, e.g., Tsukamoto & Machida 2011; Tsukamoto et al. 2015). Therefore, we conclude that the angular momentum of the first core depend more strongly on the initial condition of the molecular cloud cores (see, e.g., Joos, Hennebelle & Ciardi 2012).

4.3 Formation of the protostar

When the central density reaches $\rho_c \sim 10^{-3}$ g cm $^{-3}$ and the hydrogen molecules are completely dissociated, the gas evolves adiabatically and the protostar forms at the centre of the first core. In figure 7, we show the cross sections of density, temperature, and plasma β around the protostar. The central density is $\rho_c \sim 10^{-3}$ g cm $^{-3}$ at this epoch and just after the protostar formation. Note that the x , y , and color-bar scales differ between the ideal model and resistive models because the structure around the protostar in the ideal model is quantitatively different from the one in the other models. The density distributions of the resistive models (middle and bottom left panels) exhibit the dumbbell-like structures. These structures indicate that the rotation plays a role in the resistive models. On the other hand, in model 1 (the ideal model), the density structure is elliptical and there is no dumbbell-like structure even in vicinity of the protostar. As we will show below, the rotationally supported disc quickly forms during the subsequent evolution in the resistive models but does not form in the ideal model. The temperature distributions around the protostar are smooth and roughly spherically symmetric in all models. The temperature exceeds 1000 K and the magnetic diffusion is no longer effective in the entire region. In the model 2, the low β region forms in the vertical direction. This structure is created by the rotational amplification of the magnetic field. As a result, the plasma β becomes $\beta \sim 10^{-1}$. The magnetic field is also magnified in model 3. However, it is not a significant magnification and the plasma β in the vertical direction is still $\beta \sim 10^2$ at this epoch. We cannot find any signature of the rotational amplification in model 1. The low β region in the vertical direction is created by a dragging of the poloidal magnetic field. The figure 7 shows that the structures around the protostar are significantly different even just after the protostar formation when the magnetic diffusion is considered.

After the protostar forms, it evolves via the mass ac-

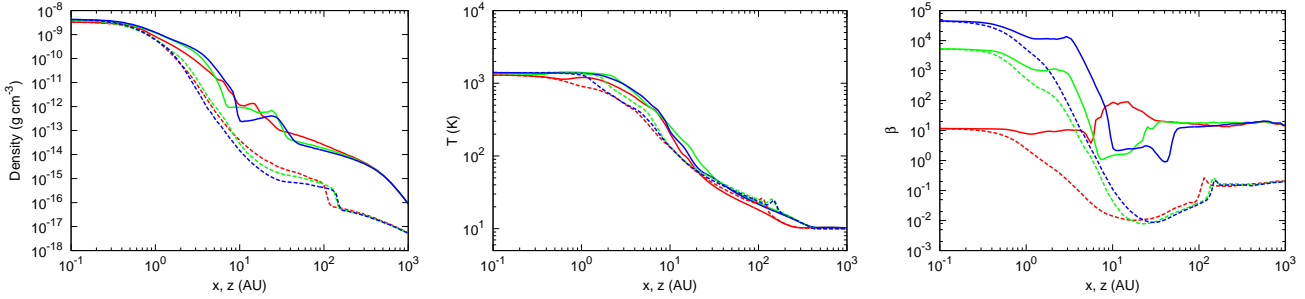


Figure 4. The density (left), gas temperature (middle), and plasma β (right) profiles. The epochs are the same as in the figure 3. The solid and dashed lines show the profiles of the x and z directions, respectively. The red, green, and blue lines show the results of model 1 (ideal model), model 2 (with Ohmic diffusion), and model 3 (with Ohmic and ambipolar diffusion), respectively.

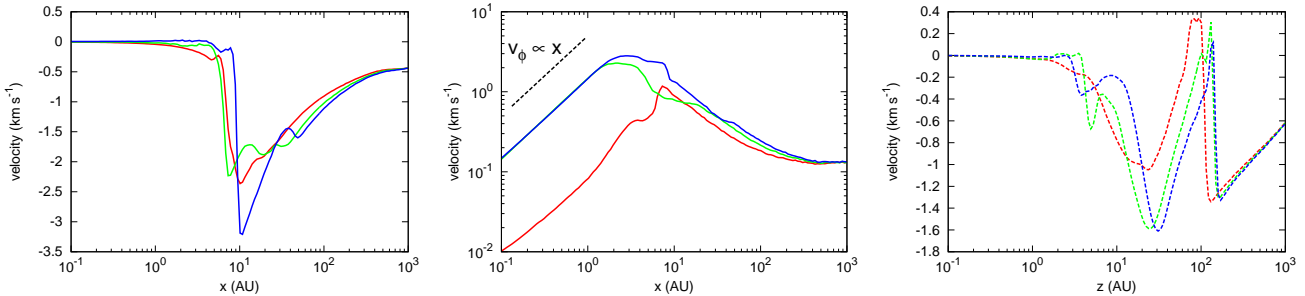


Figure 5. The profiles of the infall velocity (left) and rotation velocity (middle) in the x direction and the infall velocity in the z direction (right). The epochs are the same as in the figure 3. The red, green, and blue lines show the results of model 1 (ideal model), model 2 (with Ohmic diffusion), and model 3 (with Ohmic and ambipolar diffusion), respectively.

cretion from the remnant of the first core. In figure 8, we show the density and gas temperature along the x -axis (solid lines) and z -axis (dashed lines) at the end of the simulations. The central densities and temperatures reach $\rho_c \sim 10^{-2} - 10^{-1} \text{ g cm}^{-3}$ and $T_c \gtrsim 10^4 \text{ K}$, respectively. From the decrease in the density and temperature of the red lines around $x, z \sim 10^{-2} \text{ AU}$, we can identify the radius of the protostar in the ideal model as $r \sim 10^{-2} \text{ AU}$. In the ideal model, the difference between the density in the horizontal and the vertical directions is not large and the density structure is almost spherically symmetric. On the other hand, the density profiles of the resistive models show a different structure around the protostar. After the formation of the protostar, the rotationally supported disc of size 1 AU quickly forms in resistive models in these epochs. Because of the disc formation, the boundary of the protostar becomes ambiguous in the density and temperature profiles in the horizontal direction. Weak shock wave structures can be seen at $x \sim 1 \text{ AU}$ in the green and blue solid lines of density. This is the boundary of the circumstellar discs.

In figure 9, we show the infall and rotation velocity along the x -axis. The left panel shows the infall velocity. In the ideal model, the infall reaches $x \sim 10^{-2} \text{ AU}$, which shows that the first core remnant accretes directly onto the central protostar. On the other hand, the infall stops at $x \sim 1 \text{ AU}$ in the resistive models. This radius corresponds to the shocks in the density profiles and thus to the edges of the discs. Note that there are the other shocks at $x \sim 10 \text{ AU}$. These are the accretion shocks at the surface of the first core. The remnant of the first core still exists in these epochs.

We can see a clear transition of the rotation profile at

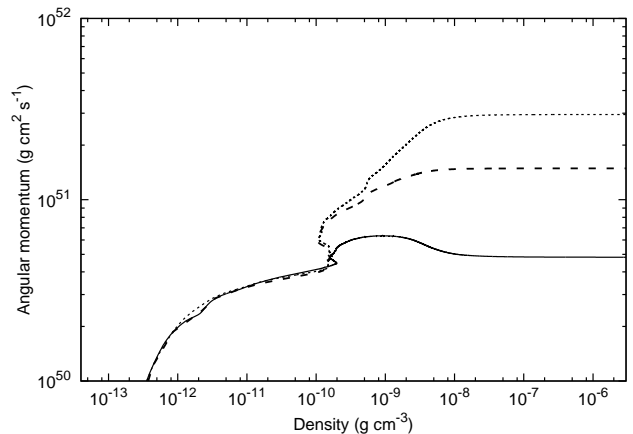


Figure 6. The evolution of the angular momentum of the first core in relation to the central density. The solid, dashed, and dotted lines show the results of model 1, 2, and 3, respectively.

$x \sim 10^{-2} \text{ AU}$ in the resistive models (blue and green lines). In $x \lesssim 10^{-2} \text{ AU}$, the profile obeys $v_\phi \propto x$ and the gas rigidly rotates. This rigidly rotating region is the protostar and its radius in the resistive models is also $r \sim 10^{-2} \text{ AU}$. In $10^{-2} \lesssim x \lesssim 1 \text{ AU}$, the profile follows $v_\phi \propto x^{-0.2}$. This is the rotation profile of the disc around the protostar. The rotation profile of the disc is more shallow than for a Keplerian disc (or disc subjected to a gravitational potential created by a point mass) which obeys the profile of $v_\phi \propto x^{-0.5}$. This means that both the self-gravity of the disc and the gravity of the central protostar influence the rotation profile.

4.4 Rotationally supported disc around protostar

As we have seen above, there are several features of the density and velocity profiles which suggest the existence of a circumstellar disc. For example, the rotational velocity at the mid-plane of models 2 and 3 is considerably larger than the radial velocity in $10^{-2} \lesssim x \lesssim 1$ AU. In addition, shocks exist at $x \sim 1$ AU in the density and infall velocity profiles. However, it is not clear from the above analysis whether the disc is rotationally supported or not.

To confirm that the disc is really rotationally supported, the ratio of the sum of the centrifugal and the pressure gradient forces to the radial gravitational force,

$$q_1 = \left| \frac{v_\phi^2/r + \nabla_r p/\rho}{\nabla_r \Phi} \right|, \quad (21)$$

is plotted in figure 10 with the solid lines and the ratio of the centrifugal to the radial gravitational force,

$$q_2 = \left| \frac{v_\phi^2/r}{\nabla_r \Phi} \right|, \quad (22)$$

with the dashed lines. Here, p and Φ are the pressure and the gravitational potential, respectively. When $q_1 = 1$ and $q_2 \ll q_1$, the gas is supported by the pressure gradient force. On the other hand, when $q_1 = 1$ and $q_2 \sim q_1$, the gas is mainly supported by the centrifugal force.

The red lines show that $q_1 \sim 1$ and $q_2 \ll q_1$ for $x \lesssim 10^{-2}$ AU. This means that a pressure supported second core (the protostar), whose radius is $r \sim 10^{-2}$ AU exists at the centre. On the other hand, the radial gravitational force always dominates other forces for 10^{-2} AU $\lesssim x \lesssim 5$ AU. Therefore, neither the pressure gradient force nor the centrifugal force can cancel the gravitational collapse and no rotationally supported disc forms in the ideal model. On the other hand, the green and blue lines show that q_1 is almost unity for $x \lesssim 1$ AU and the gravitational force is cancelled in this region. For $x \lesssim 10^{-2}$ AU, the $q_1 \sim 1$ and $q_2 \ll q_1$, which shows the existence of a pressure supported protostar. Meanwhile, q_2 is about 0.6 for 10^{-2} AU $\lesssim x \lesssim 1$ AU and 60% of the gravitational force is cancelled by the centrifugal force and the remaining 40% is cancelled by the pressure gradient force in this region. Thus, the gas is supported mainly by the centrifugal force. From these results, we conclude that the rotationally supported disc forms naturally in the very early phase of the protostar formation when the magnetic resistivity is included and the first core phase is considered correctly. Note that the dips of the green and blue solid lines at the edge of the disc are due to the large pressure gradient there. The ram pressure caused by the mass accretion should balance this.

The first core directly becomes the disc and its mass is much larger than that of the protostar during its formation epoch. Thus, it is expected that the self gravity plays an important role in the early phase of the disc evolution (Inutsuka, Machida & Matsumoto 2010). In figure 11, we show Toomre's Q value of the disc $Q = \frac{c_s \Omega}{\pi G \Sigma}$, where we approximate the epicycle frequency κ as Ω . In the disc region 10^{-2} AU $\lesssim x \lesssim 1$ AU Toomre's Q value is $Q \sim 2 - 3$. As pointed out in previous studies, the disc becomes unstable against non-axisymmetric perturbations when $Q \sim 1.5$ and the spiral arms develop (Laughlin, Korchagin & Adams 1998). The spiral arms invoke an angular momentum trans-

fer. Although, the Q value is still slightly larger than 1.5, it is expected that the gravitational instability plays a very important role for the angular momentum transfer in the subsequent disc evolution because a large amount of the remnant of the first core is still accreting to the disc and the disc mass increases quickly.

5 SUMMARY AND DISCUSSIONS

In this paper, we investigated the formation and evolution of the first core, the protostar and the disc around the protostar by using three-dimensional simulations with radiation transfer, as well as Ohmic and ambipolar diffusions.

Our findings are summarized as follows.

(i) The magnetic flux is largely removed in the first core phase. As a result, at the centre of the first core, plasma β becomes $\beta > 10^4$. On the other hand, the β at the centre of the first core in ideal simulation is $\beta \sim 10$.

(ii) Even though the plasma β inside the first core is significantly different in the resistive and the ideal models, the angular momentum of the first core is not (within an order of magnitude). This is because most of the angular momentum has been removed before the magnetic diffusion processes play a role. Actually, figure 11 of Machida, Inutsuka & Matsumoto (2007) suggests that most of the angular momentum is removed from the gas during the isothermal collapse phase. When the magnetic field is neglected, a disc with $r \sim 100$ AU forms in the cloud core for the parameters adopted in our simulations (see, e.g., Tsukamoto & Machida 2011; Tsukamoto et al. 2015). This also suggests that most of the angular momentum is removed during the isothermal phase.

(iii) With magnetic diffusions, a circumstellar disc forms around the protostar just after protostar formation even with a relatively strong initial magnetic field (we employ a uniform density sphere and an initial mass-to-flux ratio relative to the critical value of $\mu = 4$). We confirmed that the disc is rotationally supported. The disc is massive enough to enable gravitational instability to develop in the subsequent disc evolution. Thus, the gravitational instability plays an important role in the early evolution of the circumstellar discs.

The reason why most of the angular momentum is removed from the gas in the isothermal collapse phase can be understood by comparing the magnetic braking timescale $t_b \sim \lambda_J/v_A$ to the free-fall timescale t_{ff} , where λ_J and v_A are the Jeans length and Alfvén velocity, respectively. The magnetic braking timescale is estimated as the time in which the inertia of the central region is equal to the inertia of the envelope where the Alfvén wave sweeps (Matsumoto & Tomisaka 2004). The ratio of the two timescale t_b/t_{ff} is given as $t_b/t_{\text{ff}} \sim \lambda_J/(v_A t_{\text{ff}}) \sim \sqrt{\beta}$. In our simulations, the plasma β is $\beta = 1.7$ at the initial condition ($\rho = 5.5 \times 10^{-18}$ g cm $^{-3}$) and decreases during the early isothermal collapse phase as $\beta \propto c_s^2/v_A^2 \propto \rho^{-1/3}$, where we assume that c_s is constant and $B \propto \rho^{2/3}$ as shown in figure 2. When the central density reaches $\rho_c = 10^{-15}$ g cm $^{-3}$, $t_b/t_{\text{ff}} = \sqrt{\beta} = 0.71$ and the magnetic braking timescale becomes shorter than the free fall timescale. Therefore, $t_b/t_{\text{ff}} \lesssim 1$ and the angular mo-

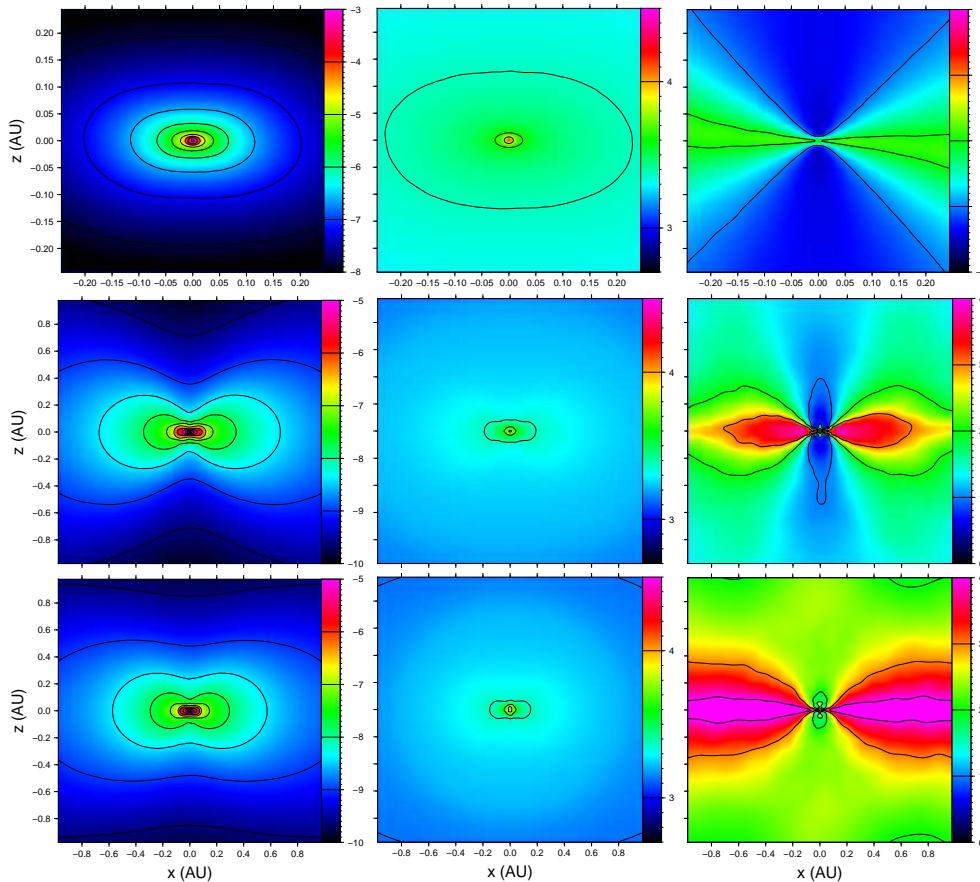


Figure 7. The cross sections of the density, gas temperature, and plasma β (from left to right) around the protostar in the $y = 0$ plane. The top, middle, and bottom row corresponds to model 1, 2, and 3, respectively. The thin black lines show the contours of each quantity. The color bars of the density, temperature, and plasma β are expressed as $\log(\rho [\text{g cm}^{-3}])$, $\log(T [\text{K}])$, and $\log(\beta)$, respectively. Note that the x , y , and color-bar scales differ between the ideal model and the resistive models.

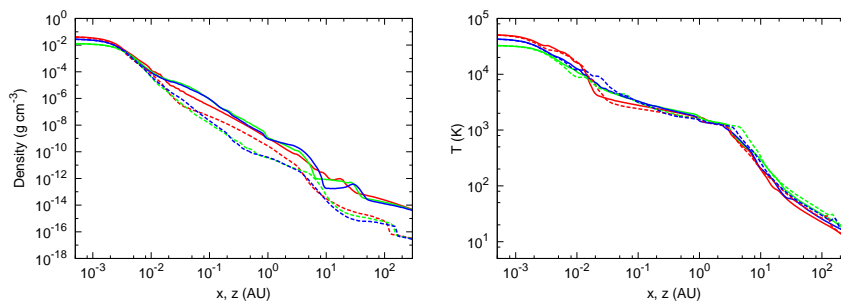


Figure 8. The profiles of the density (left) and gas temperature (right) at the end of the simulations. The solid and dashed lines show the profiles in the x and z directions, respectively. The red, green, and blue lines show the results of model 1, 2, and 3, respectively.

mentum is largely removed during the isothermal collapse phase.

Our results about the disc formation are largely consistent with those of the previous studies which followed the protostar formation with sufficient resolution and considered the first core phase (e.g., Machida & Matsumoto 2011; Tomida et al. 2013). We believe that the development of a disc at the very early phase of the star formation is a robust consequence. The previous research we mentioned above considered only Ohmic diffusion. On the other hand, we also included ambipolar diffusion. This does not change

the overall formation process of the disc significantly. However, it is possible that the ambipolar diffusion plays a more important role in the subsequent evolution of the disc because it extends the density range in which the magnetic field and the gas are decoupled and allows the magnetic flux to escape from the disc.

The difference in disc formation between the ideal model and resistive models is due to the strength of the magnetic field and not the difference in the angular momentum of the first core. In our simulations, the circumstellar disc forms in the resistive models (model 2 and 3) and does

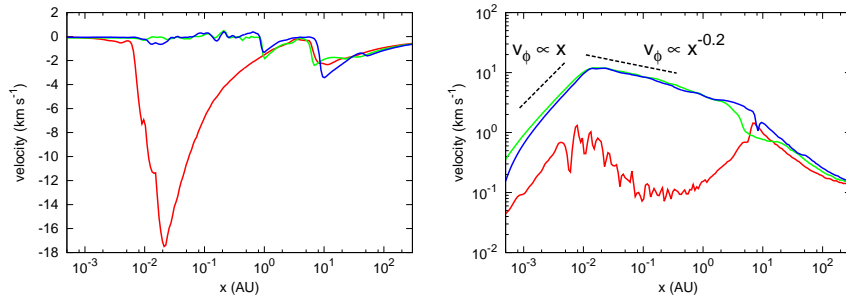


Figure 9. The profiles of the infall velocity (left) and rotation velocity (right) in the x direction. The epochs are the same as in figure 8. The red, green, and blue lines are also defined as in figure 8.

not in the ideal model (model 1). As we have seen above, in resistive models, the plasma β of the envelope around the protostar is $\beta \gtrsim 10^1$ except for the vicinity of the protostar of model 2 (the middle and bottom right panels of figure 7) and the magnetic braking is ineffective. On the other hand, the magnetic field removes the angular momentum from the gas during the second collapse in the ideal model because the plasma β of envelope is $10^{-1} < \beta < 10^1$ (see, the top right panel of figure 7) and the magnetic braking timescale is comparable or less than the free-fall timescale ($t_b/t_{\text{ff}} \sim \sqrt{\beta}$). This is why the circumstellar disc does not form in the ideal model. The simulation with Ohmic diffusion in Tomida, Okuzumi & Machida (2015) showed that the circumstellar disc forms even in the slowly rotating first core ($J \sim 2 \times 10^{50} \text{ g cm}^2 \text{ s}^{-1}$ where J is the angular momentum). Thus, the several-fold difference in the angular momentum does not affect whether or not the disc forms.

Because the magnetic flux is largely removed in the first core phase, the proper treatment of the first core is necessary to investigate the formation of the protostar and disc. In previous works which argue that the disc formation is strongly suppressed by the magnetic braking (e.g., Mellon & Li 2008; Li, Krasnopolsky & Shang 2011), the inner boundary was set from the beginning of the simulations. With this treatment, the previous works cannot follow the first core phase properly that should be supported by gas pressure. The discrepancy between our results and those of these works should be due to the different treatments of the first core phase (see, also Dapp, Basu & Kunz 2012).

It is expected that the disc size becomes larger than the size obtained in our simulations ($r < 1 \text{ AU}$) once the mass accretion from the remnant of the first core finishes because the massive remnant still exists and is accreting onto the disc, even at the end of the simulations. Unfortunately, it is almost impossible to investigate the further evolution of the disc without a sink. Although the sink may introduce numerical artefacts (especially in the few sink radius), it is an essential technique for investigating the long-term evolution of the disc. We will investigate the further evolution of the disc with the sink technique while remembering that this introduces numerical artefacts.

In this paper, we showed that the SPH method is capable of treating MHD and non-ideal processes in realistic astrophysical simulations. Our results are largely consistent with those of the recent non-ideal RMHD simulations with the static-mesh-refinement code (Tomida, Okuzumi & Machida 2015). Thus, our method is

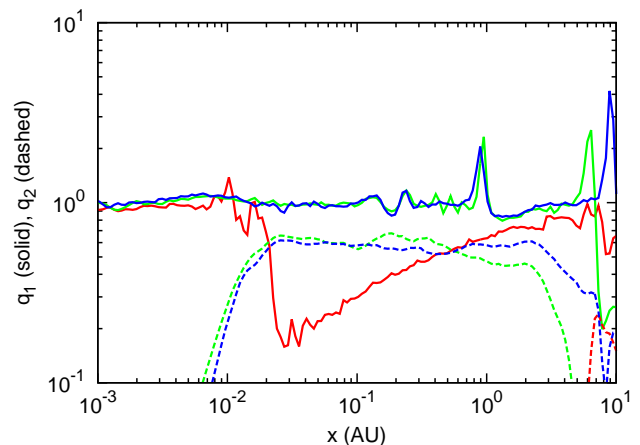


Figure 10. Solid lines show the ratio of the sum of the centrifugal force and the pressure gradient force to the radial gravitational force, $q_1 = \left| \frac{v_\phi^2/r + \nabla_r p/\rho}{\nabla_r \Phi} \right|$, as a function of the radius. Here, p and Φ are the pressure and the gravitational potential, respectively. The dashed lines show the ratio of the centrifugal force to the radial gravitational force, $q_2 = \left| \frac{v_\phi^2/r}{\nabla_r \Phi} \right|$. The red, green, and blue lines show the results of models 1, 2, and 3, respectively. The epochs are the same as in figure 8.

reliable and can be used for astrophysical simulations. Because the SPH method is relatively easily implemented and more flexible than static-mesh-refinement code, it can be used as an alternative method for many astrophysical problems in which the magnetic field play the important role.

In the simulations presented in this paper, several approximations were adopted. The influences of these simplifications should be investigated in future studies. For example, we used a fixed dust grain size of $a = 0.035 \mu\text{m}$ and a fixed the cosmic-ray ionization of $\xi_{\text{CR}} = 10^{-17} \text{ s}^{-1}$. The latter is not good approximation for the dense region, $\rho \sim 10^{-11} \text{ g cm}^{-3}$. We also used a simple rigidly rotating gas sphere as the initial condition. As Joos, Hennebelle & Ciardi (2012) and Machida, Inutsuka & Matsumoto (2014) have pointed out, the initial density profile and the magnetic field configuration strongly affect the size of the circumstellar discs. In future, we will investigate how the differences in the initial configuration affect the disc evolution.

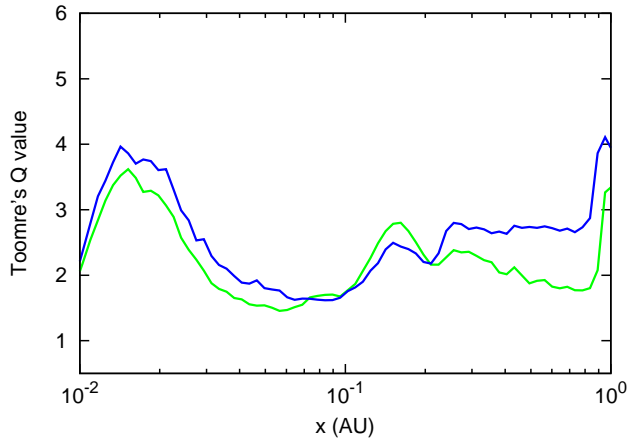


Figure 11. Toomre's Q value as a function of the radius in the x direction. The green and blue lines show the results of model 2 and 3, respectively. The epochs are the same as in figure 8.

ACKNOWLEDGMENTS

We thank Dr. K. Tomida, Dr. T. Matsumoto, and Dr. D. Stamatellos for their fruitful discussions. We also thank Dr. K. Tomida and Dr. Y. Hori to provide their EOS table to us. We also thank anonymous referee for helpful comments. The computations were performed on a parallel computer, XC30 system at CfCA of NAOJ. Y.T. and K.I are financially supported by Research Fellowships of JSPS for Young Scientists.

REFERENCES

- Alexiades V., Amiez G., Gremaud P.-A., 1996, *Com. Num. Meth. Eng.*, 12, 12
- Barnes J., Hut P., 1986, *Nature*, 324, 446
- Bate M. R., 1998, *ApJ*, 508, L95
- , 2010, *MNRAS*, 404, L79
- , 2011, *MNRAS*, 417, 2036
- Bate M. R., Tricco T. S., Price D. J., 2014, *MNRAS*, 437, 77
- Dapp W. B., Basu S., Kunz M. W., 2012, *A&A*, 541, A35
- Ferguson J. W., Alexander D. R., Allard F., Barman T., Bodnarik J. G., Hauschildt P. H., Heffner-Wong A., Tamanai A., 2005, *ApJ*, 623, 585
- Heiles C., Troland T. H., 2005, *ApJ*, 624, 773
- Hennebelle P., Fromang S., 2008, *A&A*, 477, 9
- Inutsuka S., Machida M. N., Matsumoto T., 2010, *ApJ*, 718, L58
- Iwasaki K., Inutsuka S., 2011, *MNRAS*, 418, 1668
- Iwasaki K., Inutsuka S.-I., 2013, in *Astronomical Society of the Pacific Conference Series*, Vol. 474, *Numerical Modeling of Space Plasma Flows (ASTRONUM2012)*, Pogorelov N. V., Audit E., Zank G. P., eds., p. 239
- Joos M., Hennebelle P., Ciardi A., 2012, *A&A*, 543, A128
- Larson R. B., 1969, *MNRAS*, 145, 271
- Laughlin G., Korchagin V., Adams F. C., 1998, *ApJ*, 504, 945
- Li Z.-Y., Krasnopolsky R., Shang H., 2011, *ApJ*, 738, 180
- Machida M. N., Inutsuka S., Matsumoto T., 2007, *ApJ*, 670, 1198
- Machida M. N., Inutsuka S.-i., Matsumoto T., 2008, *ApJ*, 676, 1088
- Machida M. N., Inutsuka S.-I., Matsumoto T., 2011, *PASJ*, 63, 555
- Machida M. N., Inutsuka S.-i., Matsumoto T., 2014, *MNRAS*, 438, 2278
- Machida M. N., Matsumoto T., 2011, *MNRAS*, 413, 2767
- Masunaga H., Inutsuka S., 2000, *ApJ*, 531, 350
- Matsumoto T., Tomisaka K., 2004, *ApJ*, 616, 266
- Mellon R. R., Li Z.-Y., 2008, *ApJ*, 681, 1356
- Mouschovias T. C., Paleologou E. V., 1979, *ApJ*, 230, 204
- Mouschovias T. C., Spitzer, Jr. L., 1976, *ApJ*, 210, 326
- Nakano T., Nishi R., Umebayashi T., 2002, *ApJ*, 573, 199
- Okuzumi S., 2009, *ApJ*, 698, 1122
- Price D. J., Tricco T. S., Bate M. R., 2012, *MNRAS*, 423, L45
- Semenov D., Henning T., Helling C., Ilgner M., Sedlmayr E., 2003, *A&A*, 410, 611
- Tomida K., Okuzumi S., Machida M. N., 2015, *ApJ*, 801, 117
- Tomida K., Tomisaka K., Matsumoto T., Hori Y., Okuzumi S., Machida M. N., Saigo K., 2013, *ApJ*, 763, 6
- Tomisaka K., 2002, *ApJ*, 575, 306
- Troland T. H., Crutcher R. M., 2008, *ApJ*, 680, 457
- Tsukamoto Y., Iwasaki K., Inutsuka S.-i., 2013, *MNRAS*, 434, 2593
- Tsukamoto Y., Machida M. N., 2011, *MNRAS*, 416, 591
- , 2013, *MNRAS*, 428, 1321
- Tsukamoto Y., Machida M. N., Inutsuka S., 2013, *MNRAS*, 436, 1667
- Tsukamoto Y., Takahashi S. Z., Machida M. N., Inutsuka S., 2015, *MNRAS*, 446, 1175
- Vaytet N., Audit E., Chabrier G., Commerçon B., Masson J., 2012, *A&A*, 543, A60
- Vaytet N., Chabrier G., Audit E., Commerçon B., Masson J., Ferguson J., Delahaye F., 2013, *A&A*, 557, A90
- Wardle M., 2007, *Ap&SS*, 311, 35
- Wardle M., Ng C., 1999, *MNRAS*, 303, 239
- Whitehouse S. C., Bate M. R., 2004, *MNRAS*, 353, 1078
- , 2006, *MNRAS*, 367, 32
- Whitehouse S. C., Bate M. R., Monaghan J. J., 2005, *MNRAS*, 364, 1367
- Wurster J., Price D., Ayliffe B., 2014, *MNRAS*, 444, 1104